



Cite this: DOI: 10.1039/d4ee00109e

## Dual-anion chemistry synchronously regulating the solvation structure and electric double layer for durable Zn metal anodes†

Rong Huang,‡<sup>a</sup> Jingwei Zhang,‡<sup>a</sup> Wei Wang,<sup>a</sup> Xiaohong Wu,<sup>b</sup> Xuelong Liao,<sup>a</sup> Tiantian Lu,<sup>a</sup> Youzeng Li,<sup>a</sup> Jialei Chen,<sup>a</sup> Shan Chen,<sup>a</sup> Yu Qiao, <sup>b</sup> Qing Zhao \*<sup>a</sup> and Huan Wang \*<sup>a</sup>

The zinc (Zn) metal electrode suffers from poor stability especially at high currents and large capacities due to insufficient  $Zn^{2+}$  supply and intricate side reactions. Despite significant progress, the fundamental understanding of the correlation between anions and the induced electrode/electrolyte interface remains elusive. Herein, a comparative framework based on anion-polarity hybridization is constructed, generating variations of regulation in the bulk solvation and interfacial structure. Herein, a dual-anion electrolyte towards the durable Zn electrode is modulated by incorporating the strong-polarity acetate anion ( $Ac^-$ ) together with the trifluoromethanesulfonate anion ( $OTf^-$ ), which synchronously prompts anion enrichment in the solvation structure and abundant  $Zn^{2+}$  aggregation in the Helmholtz layer. Remarkably, a cumulative plating capacity of  $15.25\text{ A h cm}^{-2}$  ( $3050\text{ h}$ ) is harvested in the  $Zn||Zn$  symmetric cell at  $10\text{ mA cm}^{-2}$  and  $10\text{ mA h cm}^{-2}$ . Moreover, the designed electrolyte demonstrates superior adaptability to varying low temperatures and high temperature ( $60^\circ\text{C}$ ). Zn-ion hybrid capacitors and Zn-air batteries also manifest enhanced electrochemical performance, demonstrating the feasibility of dual-anion chemistry in various electrochemical devices. This study provides the fundamental principle to construct advanced electrolytes via anion chemistry for high-performance Zn-based electrochemical devices.

Received 9th January 2024,  
Accepted 26th March 2024

DOI: 10.1039/d4ee00109e

rsc.li/ees

### Broader context

Aqueous zinc (Zn) metal-based electrochemical devices (ECDs) have emerged as promising candidates for grid energy storage owing to their high safety, low cost, environmental benignity, and abundant Zn resources. However, practical Zn-based ECDs are plagued by uncontrolled dendrite growth and notorious side reactions, particularly exacerbated at high currents/capacities or extreme temperatures. Despite notable advancements in electrolyte manipulation to tackle these issues, the correlation between anionic property and the interface induced remains equivocal. We devise dual-anion electrolytes by hybridization of distinct polar anions to generate a comparative framework. Herein, a strong polar acetate anion coupled with a trifluoromethanesulfonate anion ( $OTf^-$ ) emerged as an optimal combination through synchronous regulation of the bulk solvation and interface layer. In the symmetric Zn cell, prolonged cycle life is realized at  $10\text{ mA cm}^{-2}$  and  $10\text{ mA h cm}^{-2}$ , yielding an ultrahigh cumulative plating capacity of  $15.25\text{ A h cm}^{-2}$  ( $3050\text{ h}$ ), which surpasses state-of-the-art high-capacity Zn anodes. Furthermore, low temperature adaptability and high temperature ( $60^\circ\text{C}$ ) tolerance are also enabled. Both the assembled  $Zn||AC$  hybrid capacitors and  $Zn||air$  batteries demonstrate the potential to enhance the lifespan of Zn-based ECDs. This study contributes to the fundamental principle for modulating advanced electrolytes through anion chemistry towards high-performance Zn-based electrochemical devices.

<sup>a</sup> Key Laboratory of Advanced Energy Materials Chemistry (Ministry of Education), Renewable Energy Conversion and Storage Center (RECAST), Collaborative Innovation Center of Chemical Science and Engineering (Tianjin), College of Chemistry, Nankai University, Tianjin 3000711, China.

E-mail: zhaoq@nankai.edu.cn, huan.wang0520@nankai.edu.cn

<sup>b</sup> State Key Laboratory of Physical Chemistry of Solid Surfaces, Department of Chemistry, College of Chemistry and Chemical Engineering, Xiamen University, Xiamen 361005, China

† Electronic supplementary information (ESI) available. See DOI: <https://doi.org/10.1039/d4ee00109e>

‡ R. H. and J. Z. contributed equally to this paper.

### Introduction

Aqueous zinc (Zn) metal-based electrochemical devices (ECDs) have emerged as promising candidates for large-scale energy storage owing to the intrinsic features of high safety, low cost, environmental benignity, and abundant Zn resources.<sup>1–4</sup> However, the development of aqueous Zn-based ECDs is plagued by uncontrolled dendrite growth and notorious side reactions at the electrode/electrolyte interface. It has been well

accepted that the electric double layer (EDL) consists of a compact layer and a dispersed layer. In the realm of the compact layer, the inner Helmholtz plane (IHP) arises due to the specific adsorption of electrolyte constituents, while the outer Helmholtz plane (OHP) is occupied by fully solvated cations.<sup>5</sup> Under an electric field, the solvated Zn<sup>2+</sup> gradually detaches from coordinated water, crossing the OHP to reach the IHP, followed by the electroreduction of Zn<sup>2+</sup> and intricate interference of de-solvated water decomposition in the vicinity of the Zn surface.<sup>6–9</sup> At high currents and capacities, the mismatch between the supply and consumption of Zn<sup>2+</sup> at the electrode/electrolyte interface becomes surged, posing a great challenge to achieve dendrite-free electroplating. Therefore, the EDL and solvation structure dominate the evolution of the interface, which serve as pivotal factors in determining Zn deposition behaviour and subsequent cycling capability.<sup>5,10</sup>

Electrolyte manipulation with a direct effect on the solvation structure and interfacial micro-environment has attracted extensive attention to address the issues. The current studies focus on the following three approaches: (i) employing cosolvents to substitute water and form a solid electrolyte interface (SEI) layer,<sup>11–14</sup> (ii) introducing low-concentration additives as EDL regulators to isolate reactive water from contacting the Zn electrode, constrain 2D diffusion of Zn<sup>2+</sup> and/or form a SEI;<sup>15–20</sup> (iii) constructing a “water in salt” system to decrease free water and increase contact ion pairs in favor of the anion-derived SEI.<sup>1,21,22</sup> Despite considerable advances, potential issues caused by these approaches can arise, such as compromised intrinsic safety and ionic conductivity of the aqueous electrolyte, unendurable protection, and elevated electrolyte viscosity and cost. Hence, it remains highly desirable to engineer electrolytes in pursuit of inheriting the advantages of aqueous electrolytes and enhancing the stability of the interface for sustainable Zn electrodes. Furthermore, salt anions not only compete with the solvent for coordinating Zn<sup>2+</sup> but also feature specific adsorption on the Zn surface, thereby concurrently shaping the solvation structure and EDL.<sup>23–28</sup> Nevertheless, the correlation between the anionic property and the induced interface is ambiguous. To this end, the priority is to establish selection criteria of anions for interconnecting their effect on the bulk solvation and interfacial EDL. Additionally, it is imperative to clarify that synchronous regulation of the bulk solvation and EDL is fundamental for long-life Zn electrodes.

Herein, we present a comparative and mechanistic study on engineering dual-anion electrolytes for durable Zn electrodes by anion-polarity hybridization chemistry. Zinc trifluoromethane-sulfonate (Zn(OTf)<sub>2</sub>) is chosen as the baseline salt due to its high dissociation and favorable reduction products.<sup>29</sup> Zinc acetate (Zn(Ac)<sub>2</sub>) and zinc trifluoroacetate (Zn(TFA)<sub>2</sub>) are introduced as regulatory salts for constructing a dual-anion environment with Zn(OTf)<sub>2</sub>, respectively. Notably, OTf<sup>−</sup>, Ac<sup>−</sup> and TFA<sup>−</sup> feature similar structures (Fig. S1, ESI†), which can exclude the effect of spatial configuration and valence state. Theoretical calculation and experimental characterization reveal that the strong-polarity Ac<sup>−</sup> not only participates in the formation of the primary solvation shell of Zn<sup>2+</sup> but also redistributes

the interfacial ions for a Zn<sup>2+</sup>-enriched Helmholtz layer. Meanwhile, the weak-polarity OTf<sup>−</sup> is promoted to coordinate Zn<sup>2+</sup>, capable of forming a complete and dense SEI. Benefiting from the optimized dual-anion combination, the symmetric Zn cell attains extended cycling stability at 10 mA cm<sup>−2</sup> and 10 mA h cm<sup>−2</sup>, harvesting an ultrahigh cumulative plating capacity of 15.25 A h cm<sup>−2</sup> (3050 h), exceeding state-of-the-art high-capacity Zn anodes. Furthermore, varying low temperature adaptability and hightemperature (60 °C) tolerance are demonstrated. The assembled Zn||active carbon hybrid capacitors and Zn||air batteries showcase the feasibility of enhancing the life-span of Zn-based ECDs with the designed electrolyte. This work sheds light on the fundamental mechanisms underlying dual-anion electrolytes towards durable Zn electrodes, paving the way for devising anion chemistry in metal electrode protection.

## Results and discussion

Electrostatic potential maps (ESPs) were obtained by density-functional theory (DFT) calculations to visualize the charge spatial distribution surrounding the three kinds of anions (Fig. 1a). The methyl in Ac<sup>−</sup> exerts an electron-donating effect whereas trifluoromethyl in OTf<sup>−</sup> and TFA<sup>−</sup> intensely withdraws electrons, which results in electron delocalization. Thus, Ac<sup>−</sup> reveals strong polarity, creating a higher electrostatic driving force for cation access (−5.93 eV) in comparison with weak-polarity OTf<sup>−</sup> (−4.93 eV) and medium-polarity TFA<sup>−</sup> (−5.39 eV). This gains further validation through calculating interactions of Zn<sup>2+</sup>–H<sub>2</sub>O and different Zn<sup>2+</sup>–anion pairs, among which Ac<sup>−</sup> manifests the highest binding energy with Zn<sup>2+</sup> (in absolute value), followed by Zn<sup>2+</sup>–TFA<sup>−</sup>, Zn<sup>2+</sup>–OTf<sup>−</sup> and Zn<sup>2+</sup>–H<sub>2</sub>O in descending order (Fig. 1b). Therefore, Ac<sup>−</sup> is inclined to engage in the formation of a Zn<sup>2+</sup> solvation shell by squeezing out partial water molecules, thereby preventing water-associated side reactions. Given that the high-polarity organic group is the preferential adsorption site,<sup>30</sup> Ac<sup>−</sup> is envisioned as the targeted secondary anion for synchronous regulation of the solvation structure and EDL, as discussed in the following section.

The solvation structures of different electrolytes were experimentally investigated through a series of spectroscopic characterization studies. Fourier transform infrared (FTIR) spectroscopy was first performed to unveil the solvation structure evolution of the baseline, 0.1 M Ac<sup>−</sup>-addition and 0.7 M Ac<sup>−</sup>-addition electrolytes, which are denoted as 2 OTf, 2F-01A and 2F-07A, respectively, (Fig. 1c and Fig. S3, ESI†). Note that the addition of 0.7 M regulatory salt is near the upper dissolution threshold for dual-anion electrolytes (Fig. S2, ESI†). With Zn(Ac)<sub>2</sub> powder as a reference, the difference ( $\Delta$ ) of Fourier transform infrared (FTIR) peaks between the symmetric stretching vibration ( $\sim$ 1400 cm<sup>−1</sup>) and the antisymmetric stretching vibration ( $\sim$ 1550 cm<sup>−1</sup>) of C=O can be utilized as a probe of the bonding configuration of Zn<sup>2+</sup> and Ac<sup>−</sup>. 2F-07A shows distinct characteristic C=O peaks with enhanced  $\Delta$  values in contrast to the baseline and 2F-01A, implying more monodentate coordination of Ac<sup>−</sup> with Zn<sup>2+</sup>.<sup>31</sup> In combination with solubility and

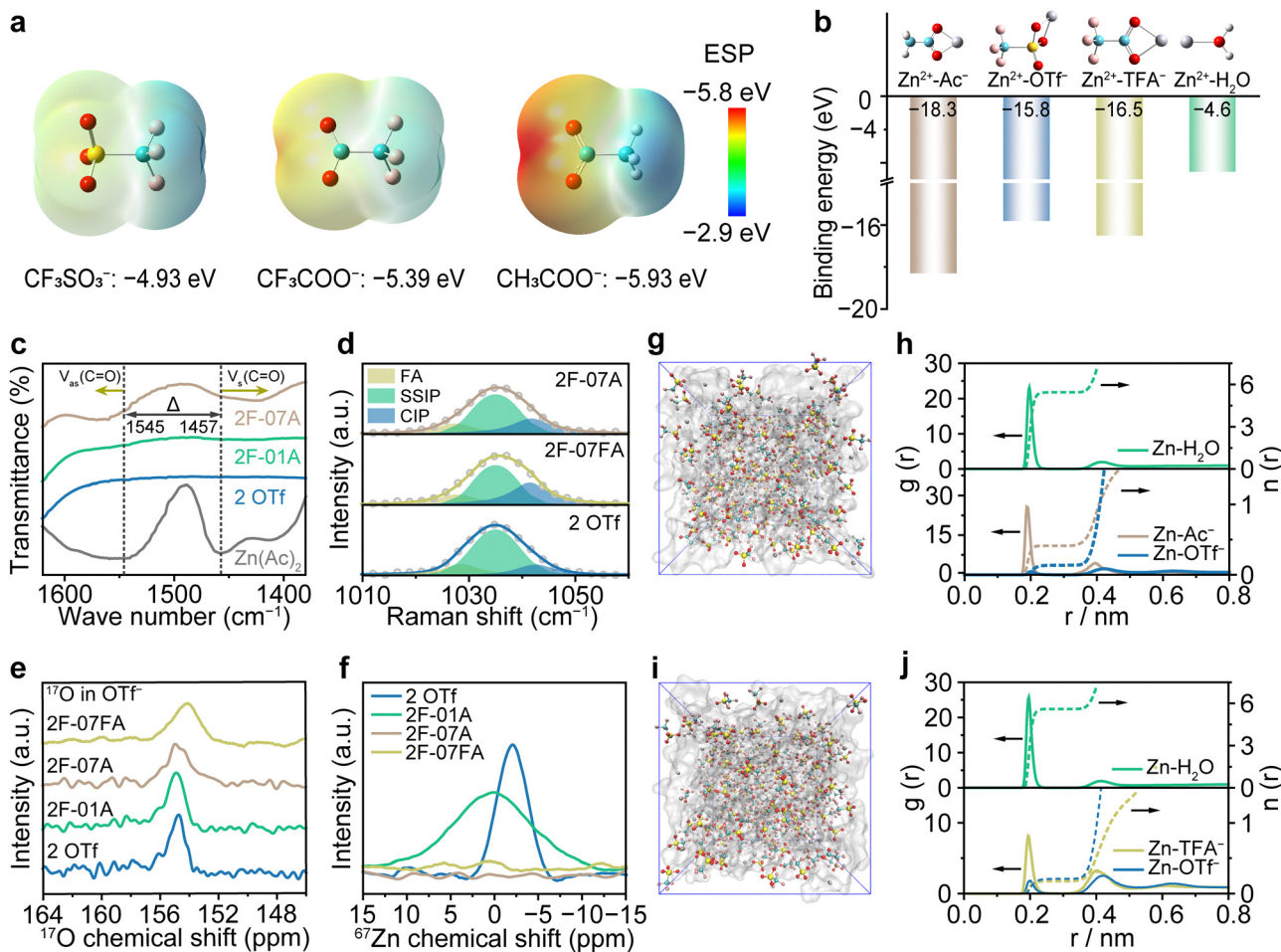


**Fig. 1** Characterization of bulk electrolytes. (a) ESP of  $\text{OTf}^-$ ,  $\text{TFA}^-$ , and  $\text{Ac}^-$ . (b) Binding energy of  $\text{Zn}-\text{H}_2\text{O}$  and different  $\text{Zn}^{2+}$ -anion pairs. (c) FTIR spectra of different electrolytes and pure  $\text{Zn}(\text{Ac})_2$  salt. (d) The fitted Raman spectra of the  $-\text{SO}_3$  stretching vibration in  $\text{OTf}^-$ . NMR spectra of (e)  $^{17}\text{O}$  and (f)  $^{67}\text{Zn}$  in different electrolytes. MD snapshots of (g) 2F-07A and (i) 2F-07FA. RDFs and coordination numbers of (h) 2F-07A and (j) 2F-07FA.

the ability to penetrate the solvation sheath of  $\text{Zn}^{2+}$ , 0.7 M was preliminarily identified as the optimal concentration of  $\text{Ac}^-$ -containing electrolytes. To persuasively assess the impacts of the dual-anion concentration and anion polarity on the electrochemical performance and the underlying mechanism, we introduced a low concentration 0.1 M  $\text{Ac}^-$ -regulated electrolyte (2F-01A) and a 0.7 M medium polarity  $\text{TFA}^-$ -regulated electrolyte (2F-07FA) in the subsequent analysis. The distinct management of these electrolytes in the bulk solvation and the interfacial EDL was also demonstrated thereafter.

The O-H stretching vibration of  $\text{H}_2\text{O}$  in FTIR is decoupled into strong H-bonds ( $\sim 3280 \text{ cm}^{-1}$ ), medium H-bonds ( $\sim 3470 \text{ cm}^{-1}$ ) and weak-H bonds ( $3580 \text{ cm}^{-1}$ ). With regulatory anions added to the baseline electrolyte, strong H-bonds slightly increase following the order of 2F-07A > 2F-07FA > 2F-01A. While for medium H-bonds and weak H-bonds, the reversed trend is observed, which is ascribed to the decreased capability of H-bond formation between the anion and  $\text{H}_2\text{O}$  in the order of  $\text{Ac}^-$ ,  $\text{TFA}^-$  and  $\text{OTf}^-$  (Fig. S4, ESI†). In Raman spectra, the  $-\text{SO}_3$  stretching band of  $\text{OTf}^-$  can be divided into free anions (FAs,  $\text{OTf}^-$ ) at  $\sim 1028 \text{ cm}^{-1}$ , solvent-separated ion pairs (SSIP,  $\text{Zn}^{2+}-\text{H}_2\text{O}-\text{OTf}^-$ ) at  $\sim 1035 \text{ cm}^{-1}$  and

contact ion pairs (CIP,  $\text{Zn}^{2+}-\text{OTf}^-$ ) at  $\sim 1042 \text{ cm}^{-1}$  (Fig. 1d and Fig. S5–S7, ESI†).<sup>32,33</sup> The CIP ratio decreases in the order of 2F-07FA > 2F-07A > 2F-01A > 2OTf due to the differences in the entropy effect and involved solvent numbers (Table S1, ESI†).  $^1\text{H}$  nuclear magnetic resonance spectroscopy ( $^1\text{H}$  NMR) exhibits an upfield shift as regulatory anions are added into both water and the baseline, which is attributed to the decrease of the electron cloud density around the hydrogen nucleus caused by the special coordination environment regulated by  $\text{Ac}^-$  and  $\text{TFA}^-$  (Fig. S8, ESI†). Meanwhile, the  $^{17}\text{O}$  NMR of  $\text{OTf}^-$  resonance becomes broader and weaker with regulatory salt addition, indicative of more  $\text{OTf}^-$  squeezing into the  $\text{Zn}^{2+}$  solvation sheath in optimal dual-anion electrolytes, evidencing the Raman findings in Fig. 1e. The negligible characteristic peaks in the  $^{67}\text{Zn}$  NMR spectra in both 2F-07A and 2F-07FA electrolytes suggest a significantly declined  $\text{Zn}^{2+}$  exchange rate during the acquisition time, further confirming the anion-enriched coordination environment (Fig. 1f).<sup>34</sup>

Molecular dynamics (MD) simulations in conjunction with corresponding radial distribution functions (RDFs) and coordination number (CN) were then performed to probe the

evolution of the  $Zn^{2+}$ -solvation structure (Fig. 1g–j and Fig. S9 and S10, ESI<sup>†</sup>). For the baseline electrolyte of 2 M  $Zn(OTf)_2$ ,  $Zn^{2+}$  is primarily surrounded by six water molecules with a sharp peak at 2 Å corresponding to the distance of  $Zn-H_2O$  pairs. In  $Ac^-$ -containing electrolytes, a distinct coordination peak located at 1.9 Å emerges, verifying a stronger interaction of  $Ac^-$ - $Zn^{2+}$  than that of  $H_2O-Zn^{2+}$ . Upon elevating the  $Zn(Ac)_2$  concentration from 0.1 M to 0.7 M, the CN of  $Ac^-$  and  $OTf^-$  increases from 0.079 to 0.448 and from 0.117 to 0.145, respectively, accompanied by a decrease in coordinated water. While for the  $TFA^-$ -containing electrolyte, 0.403 of  $TFA^-$  and 0.358 of  $OTf^-$  enter the first solvation shell of  $Zn^{2+}$ . Apparently, dual-anion electrolytes promote the evolution of the anion-enriched solvation structure, which is found to be advantageous for an anion-induced SEI, as discussed later. H-bonds were also simulated in Fig. S11 (ESI<sup>†</sup>), which shows a substantial decrease in 0.7 M-addition dual-anion electrolytes. Anion squeezing into the solvated structure with 0.7 M regulatory salt addition is statistically presented in Fig. S12 (ESI<sup>†</sup>), showing that  $OTf^-$  and regulatory anions exist in the solvation structure

of  $Zn^{2+}$ , respectively. The calculated Gibbs free energy for different solvation shells of  $Zn^{2+}$  incorporating single anion participation is shown in Fig. S13 (ESI<sup>†</sup>), following the order of  $Zn(H_2O)_5OTf^- < Zn(H_2O)_5TFA^- < Zn(H_2O)_5Ac^-$  (in absolute value), which well explains the crucial role of anion polarity in shaping the  $Zn^{2+}$ -solvation sheath.

Besides modulating the solvation structure of  $Zn^{2+}$ , the regulatory anions with strong polarity would preferentially adsorb on the Zn metal surface and manipulate IHP, thus directing the Zn deposition pattern. To this end, the ability of anions to donate electrons was investigated by the molecular orbital level to evaluate the adsorption priority.<sup>35,36</sup> As summarized in Fig. 2a,  $Ac^-$  has the highest value of the highest occupied molecular orbital (HOMO) due to the presence of electron-rich oxygen atoms, in favor of transferring electrons to the metal surface atoms, which implies the potential of  $Ac^-$  as the IHP regulator. Adsorption energy ( $E_{ad}$ ) was subsequently calculated using DFT to determine the adsorption preference of these anions and water molecules on the Zn(101) facet (Fig. 2b and Fig. S14, ESI<sup>†</sup>).  $Ac^-$  has a higher interaction with a Zn slab

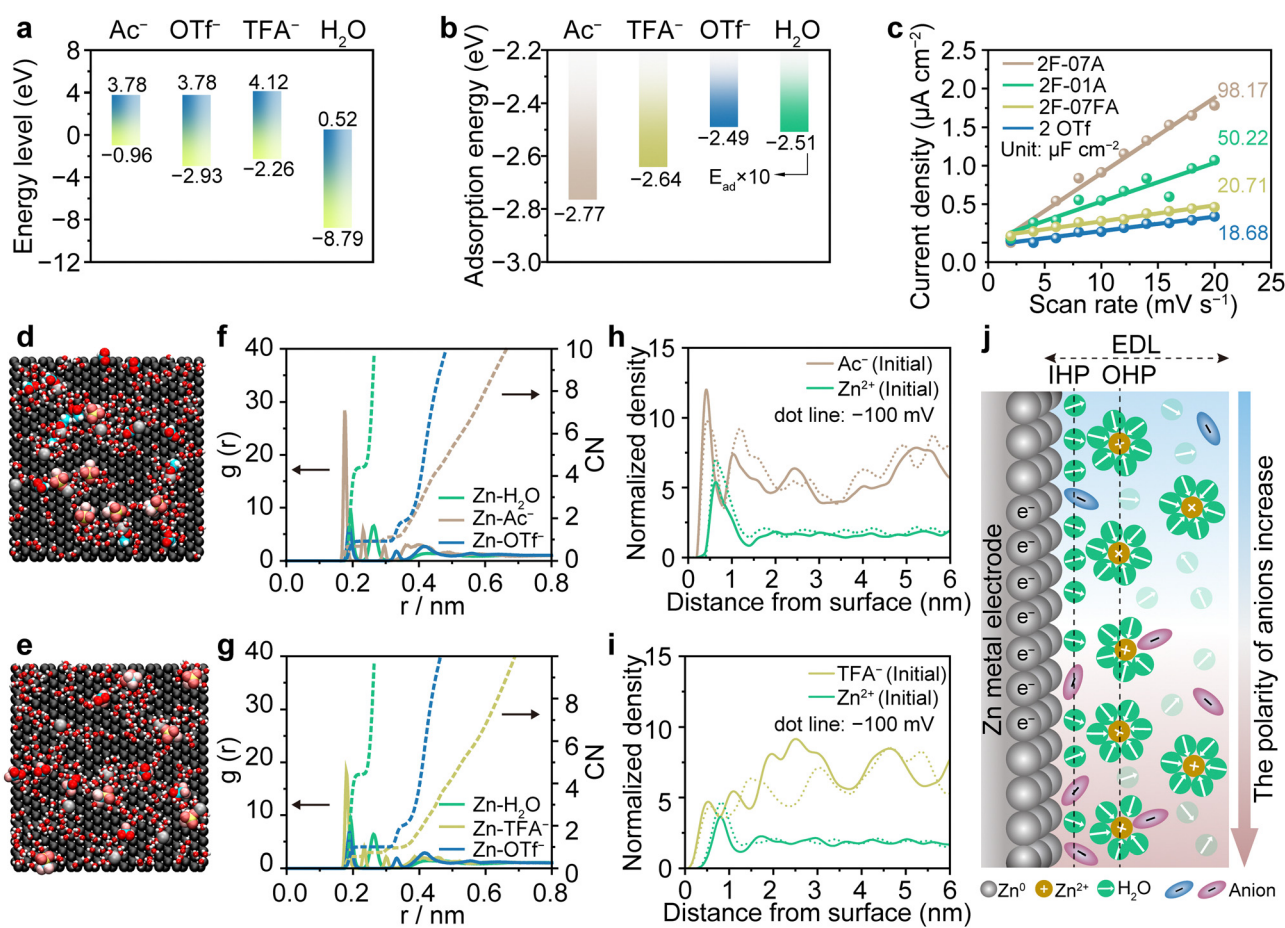


**Fig. 2** Calculation and characterization of the anion distribution and solvation structure at the electrode/electrolyte interface in the dual-anion electrolytes. (a) LUMO and HOMO energy levels of  $H_2O$  and different anions. (b) The adsorption energy of different anions and water molecules on the Zn(101) plane. (c) Plots of capacitive currents versus scan rates resulting from the corresponding CV curves. Image snapshots of the adsorbed species on the Zn electrode in the initial state in the (d) 2F-07A electrolyte and (e) 2F-07FA electrolyte. The RDF and CN of the (f) 2F-07A electrolyte and (g) 2F-07FA electrolyte. Normalized density profiles of  $Zn^{2+}$  and regulatory anions within EDL in the (h) 2F-07A electrolyte and (i) 2F-07FA electrolyte with/without a bias voltage. (j) Schematic diagram of interfacial ions induced by different polar anions.

showing an  $E_{ad}$  value of  $-2.77$  eV in comparison with other anions ( $-2.64$  eV for  $\text{TFA}^-$ , and  $-2.49$  eV for  $\text{OTf}^-$ ) and water molecules ( $-0.25$  eV), matching well with HOMO energy level results. The lowest zeta potential of Zn powder in 2F-07A also confirms that  $\text{Ac}^-$  accumulates more on the Zn surface than anions in other electrolytes (Fig. S15, ESI $\dagger$ ). Moreover, the electric double layer capacitance (EDLC) resulted from the adsorbed species and composition structure of the interface was collected by fitting cyclic voltammetry (CV) curves at different scan rates (Fig. 2c and Fig. S16, ESI $\dagger$ ).<sup>37,38</sup> It is evident that the addition of  $\text{Zn}(\text{Ac})_2$  significantly enhances the EDLC, leading to a capacitance of  $98.17\ \mu\text{F cm}^{-2}$ , which is approximately 4-fold higher than that of 2F-07FA. Since the EDLC is strongly associated with the Helmholtz layer,<sup>5</sup> it is instructive to ascertain the capacitance contribution in the Helmholtz layer.

To understand the discrepancy between  $\text{Ac}^-$  and  $\text{TFA}^-$  as regulatory anions in manipulating the EDL structure, MD simulations are employed to scrutinize the chemical structure of EDL in 2F-07A and 2F-07FA. The side-view snapshots of EDL in the simulated electrolytes are shown in Fig. S17 and S18 (ESI $\dagger$ ) and the representative top-view snapshots of the adsorbed species in the Helmholtz layer are displayed in Fig. 2d and e and Fig. S19 (ESI $\dagger$ ). The amount of the ions in the Helmholtz layer is collected in Fig. S20 (ESI $\dagger$ ). At the initial state, there is a clear surplus of  $\text{Ac}^-$  in 2F-07A compared to  $\text{TFA}^-$  in 2F-07FA, thus forming an anion-enriched interface, which can draw more  $\text{Zn}^{2+}$  to gather for charge compensation. At a bias voltage of  $-100$  mV (directed at the electroplating process), the number of  $\text{Zn}^{2+}$  transporting into the Helmholtz layer in 2F-07A surpasses that in 2F-07FA. The solvation structures of the two electrolytes in the EDL are disclosed in Fig. 2f and g, which demonstrates the enhanced anion coordination (the CN of  $\text{OTf}^-$  and both regulatory anions  $\approx 1$ ) due to the rearrangement of interfacial constituents.

Furthermore, the normalized density profiles are recorded to show the distribution of interfacial ions along the distance from the Zn electrode surface within the EDL (Fig. 2h and i). The closer distance ( $0.41$  nm) and higher density of  $\text{Ac}^-$  is accompanied by  $\text{Zn}^{2+}$  in more proximity to the Zn electrode ( $0.63$  nm), thus contributing to a more condensed Helmholtz layer, in good agreement with the significantly enhanced EDLC for 2F-07A in Fig. 2c. When the potential was applied to the two systems, the 2F-07A system showed the opposite changing trend in the number density of anions and cations located in the Helmholtz layer (within  $1$  nm of the electrode), which is more conspicuous compared to the observation in 2F-07FA. Meanwhile, both  $\text{Zn}^{2+}$  and  $\text{Ac}^-$  in 2F-07A retain a higher diffusion coefficient as compared to  $\text{Zn}^{2+}$  and  $\text{TFA}^-$  in 2F-07FA with/without a bias voltage (Fig. S21, ESI $\dagger$ ). This stark contrast suggests that the  $\text{Zn}^{2+}$ -rich interface in 2F-07A is expected to counter rapid electrode reaction consumption in the EDL, ensuring dendrite-free electrodeposition, whereas the 2F-07FA system is more inclined to conduct uneven deposition owing to the insufficient  $\text{Zn}^{2+}$  supply. In addition, 2F-07A and 2F-07FA showcase consistent levels of viscosity and ionic conductivity among the examined electrolytes (Fig. S22, ESI $\dagger$ ), underlining

the critical role of the interface structure in ion supply in electroreduction processes. Taken together, we conclude the synchronous effect of anion polarity on regulating solvation sheath and EDL structure, as illustrated in Fig. 2j. Specifically, the strong-polarity  $\text{Ac}^-$  features strong coordination and adsorption capability that is capable of generating a more condensed interface micro-environment, which is anticipated to tackle the multiple issues in Zn metal anodes.

To experimentally validate the hypothesis, chronoamperometry (CA) measurements were conducted to compare Zn deposition behavior in the investigated electrolytes (Fig. 3a). In the baseline electrolyte, a continuous increase in current response over  $1000$  s indicates rampant 2D diffusion, which accelerates dendrite growth.<sup>19</sup> In contrast, dual-anion electrolytes all manifest a steady 3D diffusion process following transient 2D diffusion, corresponding to  $200$  s for 2F-07A,  $400$  s for 2F-07FA and  $500$  s for 2F-01A, respectively. The alteration in the deposition behavior is attributed to the fact that the adsorbed anions can restrain lateral  $\text{Zn}^{2+}$  diffusion. The Tafel plots show that the 2F-07A electrolyte has the lowest exchange current density (Fig. 3b and Fig. S23, ESI $\dagger$ ), indicating the most significant reduction in the corrosion rate.<sup>39</sup> Additionally, the linear sweep voltammetry characterization and calculated LUMO energy levels in different electrolytes collectively confirm that water-related side reactions are pronouncedly inhibited in 2F-07A (Fig. S24 and S25, ESI $\dagger$ ). Accordingly, the tailored 2F-07A electrolyte demonstrates greatly improved anticorrosion ability with a smooth Zn surface after immersion (Fig. S26, ESI $\dagger$ ). Furthermore, Zn deposition dynamics was evaluated by calculating active energy for the de-solvation process *via* temperature-dependent electrochemical impedance spectroscopy (EIS) measurements (Fig. 3c and Fig. S27, ESI $\dagger$ ) based on the law of Arrhenius equation.<sup>40-42</sup> 2F-07A electrolyte manifests the lowest charge transfer resistance ( $R_{ct}$ ) at all temperatures, suggesting that strong-polarity  $\text{Ac}^-$  can facilitate the charge transfer dynamics. Besides, 2F-07A demonstrates an apparently lower active energy of  $35.9\ \text{kJ mol}^{-1}$  than its counterparts, reducing the possibility of HER occurrence in IHP.

The distribution of relaxation times (DRT) derived from EIS can further probe interface electrochemical processes with diverse relaxation times ( $\tau$ ) (Fig. 3d-g).<sup>43</sup> Within the measured temperature range, the peaks with  $\tau$  of  $\approx 10^{-3}$  to  $10^{-1}$  s and  $10^0$  to  $10^1$  s represent charge transfer and interfacial diffusion, respectively. The peak area can be converted to the impedance value. Meanwhile, the diffusion impedance increases with the order of 2F-07A (Fig. 3d), 2F-01A (Fig. 3f), 2F-07FA (Fig. 3e), and the baseline (Fig. 3g), due to changes in the concentration of  $\text{Zn}^{2+}$  at the interface. This contrast further emphasizes the capability of strong-polarity  $\text{Ac}^-$  in attracting  $\text{Zn}^{2+}$  for a more condensed interface structure.

Thus, based on theoretical simulations and experimental findings, the functions of the four electrolytes in the bulk solvation and interfacial EDL can be drawn as follows: (i) The baseline electrolyte possesses both weak regulations in the bulk and at the interface; (ii) 2F-01A exhibits robust interface regulation but modest regulation in the bulk; (iii) 2F-07FA exhibits

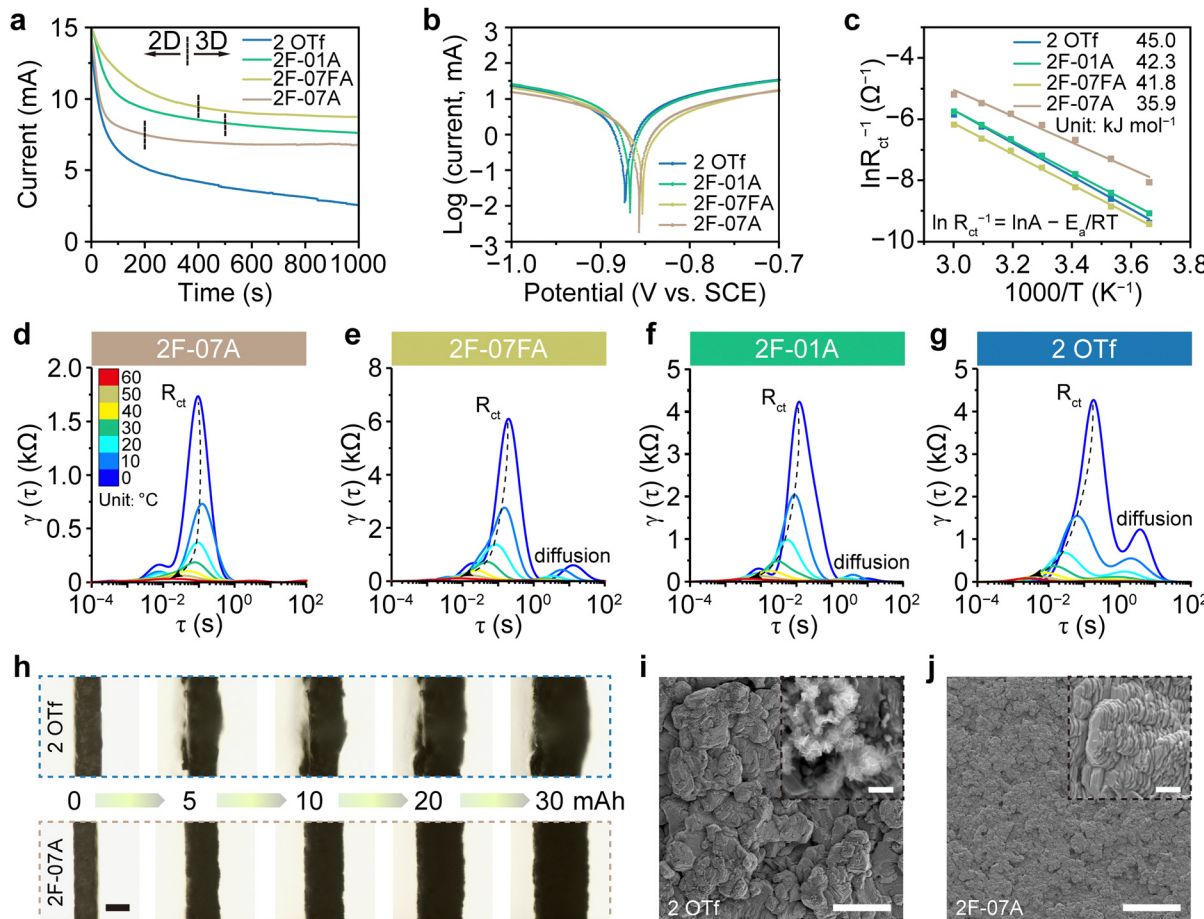


**Fig. 3** Characterization of the Zn electrode/electrolyte interface. (a) Chronoamperometric plots of Zn electrodeposition in different electrolytes with a polarization voltage of  $-150$  mV. (b) Tafel polarization curves of Zn electrodes with the baseline and dual-anion electrolytes. (c) Arrhenius plots of  $R_{ct}$  derived in Nyquist plots of Zn||Zn cells using different electrolytes. DRT profiles of EIS in (d) 2F-07A, (e) 2F-07FA, (f) 2F-01A and (g) 2 OTf electrolytes. (h) *In situ* optical microscopy images of the Zn plating process at a current density of  $5$  mA  $\text{cm}^{-2}$  in the baseline (top) and 2F-07A (bottom), scale bar:  $100$   $\mu\text{m}$ . SEM images of the Zn surface after  $30$  mA  $\text{h} \text{cm}^{-2}$  of deposition in (i) the baseline and (j) 2F-07A electrolyte, scale bar:  $100$   $\mu\text{m}$ . Insets are the corresponding high-magnification SEM images, scale bar:  $1$   $\mu\text{m}$ .

strong regulation in the bulk but weak interface regulation; (iv) 2F-07A synchronically exhibits prominent regulation in the bulk and at the interface.

*In situ* microscopy observations during the Zn plating process at  $5$  mA  $\text{cm}^{-2}$  are further conducted to confirm the merit of synchronized regulation. As shown in Fig. 3h, the baseline electrolyte appears to produce unevenly distributed protrusions after  $5$  mA  $\text{h} \text{cm}^{-2}$  of deposition. In sharp contrast, the employment of 2F-07A can greatly mitigate the dendrite growth under identical conditions and achieves a smooth surface even at a plating capacity of up to  $30$  mA  $\text{h} \text{cm}^{-2}$ . Correspondingly, the scanning electron microscopy (SEM) images after  $30$  mA  $\text{h} \text{cm}^{-2}$  of deposition display a flat and dense morphology with tightly packed bricks in 2F-07A (Fig. 3i), whereas the baseline electrolyte showcases bulk aggregates and fluffy flakes (Fig. 3j). For 2F-01A and 2F-07FA, randomly distributed by-products and dendritic Zn are also observed (Fig. S28 and S29, ESI†), which can impair the interface homogeneity during electrodeposition and in turn exacerbate dendrite growth. Meanwhile, atomic force microscopy (AFM) images of the Zn electrode after cycling in 2F-07A

at  $5$  mA  $\text{cm}^{-2}$  demonstrate a flatter surface without the observation of large flakes (Fig. S30, ESI†).

To evaluate the electrochemical performance of dual-anion electrolytes, symmetric Zn||Zn cells are examined under different conditions. Fig. 4a shows a comparison of the voltage profiles of Zn||Zn cells in different electrolytes at  $1$  mA  $\text{cm}^{-2}$  and  $1$  mA  $\text{h} \text{cm}^{-2}$ . As expected, the cell with the 2F-07A electrolyte exhibits an extended lifespan of over  $2400$  h, around  $40$ -fold enhancement as compared to the baseline one ( $\sim 60$  h). For 2F-01A and 2F-07FA electrolytes, the stable plating/stripping profile sustains  $350$  h and  $130$  h, respectively. Meanwhile, the rate performance of Zn||Zn cells was tested at varying current densities ranging from  $1$  mA  $\text{cm}^{-2}$  to  $20$  mA  $\text{cm}^{-2}$  with a fixed cycling time of  $1$  h, followed by a constant current density of  $10$  mA  $\text{cm}^{-2}$  and a capacity of  $10$  mA  $\text{h} \text{cm}^{-2}$  (Fig. 4b and Fig. S31, ESI†). The cell at the baseline short circuits at  $5$  mA  $\text{cm}^{-2}$  and  $5$  mA  $\text{h} \text{cm}^{-2}$ . In the cases of 2F-01A and 2F-07FA, the cells deliver an enhanced rate capability and fail at  $20$  mA  $\text{cm}^{-2}$ ,  $20$  mA  $\text{h} \text{cm}^{-2}$  and  $15$  mA  $\text{cm}^{-2}$ ,  $15$  mA  $\text{h} \text{cm}^{-2}$ , respectively. Contrastively, the cell using the 2F-07A electrolyte

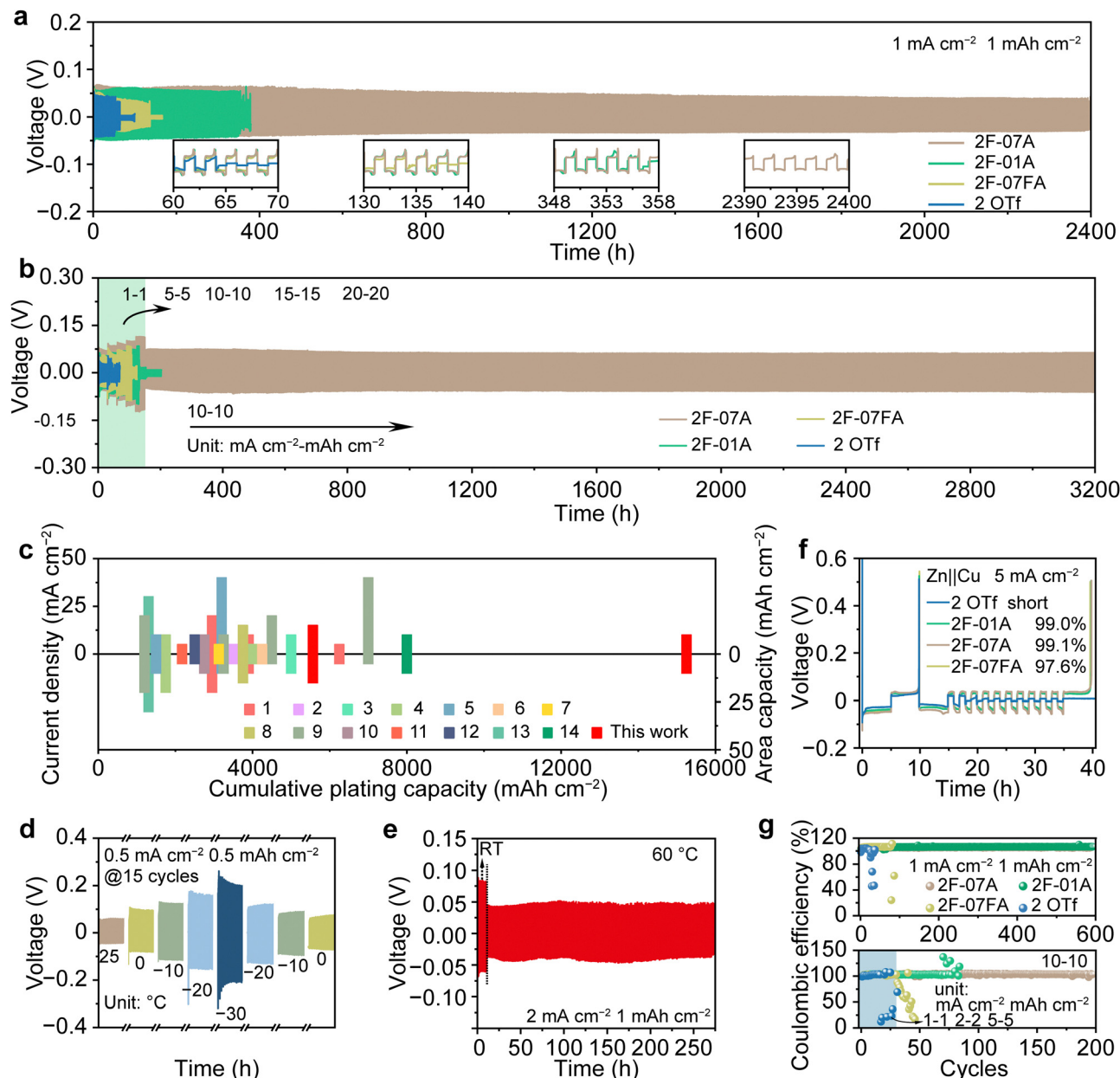


**Fig. 4** Electrochemical stability and reversibility of Zn electrodes in different electrolytes. (a) Voltage profiles of symmetric Zn cells at  $1 \text{ mA cm}^{-2}$  and  $1 \text{ mA h cm}^{-2}$ . (b) Rate performance of  $\text{Zn}||\text{Zn}$  cells. (c) Comparison of the cycling performance with those reported in recent works. (d) Varying temperature test of the  $\text{Zn}||\text{Zn}$  cell in 2F-07A ranging from  $25^\circ\text{C}$  to  $-30^\circ\text{C}$  (breakpoints correspond to the rest time) and (e) cycling at  $60^\circ\text{C}$  (RT represents room temperature). (f) Voltage–time profiles of  $\text{Zn}||\text{Cu}$  asymmetric cells at  $5 \text{ mA cm}^{-2}$ . (g) The cycling stability and reversibility of  $\text{Zn}||\text{Cu}$  cells at  $1 \text{ mA cm}^{-2}$  and  $1 \text{ mA h cm}^{-2}$  (top) and varying current densities and areal capacities (bottom).

manifests stable voltage hysteresis at all rates and can continuously cycle up to 3200 h after the test condition back to  $10 \text{ mA cm}^{-2}$  and  $10 \text{ mA h cm}^{-2}$ .

Even under rather demanding conditions of  $15 \text{ mA cm}^{-2}$  and  $15 \text{ mA h cm}^{-2}$ , the cell in the 2F-07A electrolyte enables a lifespan of 742 h (Fig. S32, ESI†). Note that high-capacity metal electrodes have garnered extensive attention for practical applications.<sup>44–46</sup> Fig. 4c and Table S3 (ESI†) compare the  $\text{Zn}||\text{Zn}$  cells using the 2F-07A electrolyte with the recently reported works on electrolyte-regulated Zn electrodes in terms

of current density, area capacity ( $\geq 5 \text{ mA h cm}^{-2}$ ) and cumulative capacity. Evidently, the 2F-07A electrolyte-equipped cell stands out with a splendid accumulative plating capacity of  $15.25 \text{ A h cm}^{-2}$  (3050 h). To simulate the intermittent operation of the cell in an actual working scenario, the cell using 2F-07A cycling is subjected to  $1 \text{ mA cm}^{-2}$  and  $1 \text{ mA h cm}^{-2}$  with 24 h intervals, which can operate for more than 6000 h (Fig. S33, ESI†). Temperature adaptability of the 2F-07A electrolyte was also examined. As shown in Fig. 4d, the cell with 2F-07A presents a stable cycling behavior even at low temperatures

down to  $-30^{\circ}\text{C}$ . After pre-cycling at room temperature (RT) to stabilize the interface, the cell with 2F-07A can stably cycle at  $2\text{ mA cm}^{-2}$  and  $1\text{ mA h cm}^{-2}$  exceeding 250 h at  $60^{\circ}\text{C}$  (Fig. 4e). These results demonstrate that the designed 2F-07A electrolyte holds great application potential over a wide temperature range.

Coulombic efficiency (CE) is a critical indicator to determine the electrode reversibility during charging/discharging cycles. A modified Aurbach method was carried out to minimize substrate interference by  $\text{Zn}||\text{Cu}$  asymmetric cells at  $5\text{ mA cm}^{-2}$  (Fig. 4f).<sup>47</sup> The cells using  $\text{Ac}^-$ -containing electrolyte reveal a high CE of 99.1% for 2F-07A and 99.0% for 2F-01A, superior to that of 2F-07FA (97.6%) and the baseline (short circuit during charging). Long-term cycling reversibility of  $\text{Zn}||\text{Cu}$  asymmetric cells was also measured for comparison. At  $1\text{ mA cm}^{-2}$  and  $1\text{ mA h cm}^{-2}$  (Fig. 4g, top and Fig. S34, ESI†), the  $\text{Ac}^-$ -containing electrolytes offer a stable CE of around 99% over 600 cycles, exceeding that using 2F-07FA (<80 cycles) and the baseline (<50 cycles). Thereupon, varying current densities ranging from  $1\text{ mA cm}^{-2}$  to  $10\text{ mA cm}^{-2}$  were applied (Fig. 4g, bottom and Fig. S35, ESI†). The 2F-07A electrolyte exhibits an average CE of 98.4% at  $10\text{ mA cm}^{-2}$  and  $10\text{ mA cm}^{-2}$  over 200 cycles, whereas drastic fluctuations are observed sequentially in the baseline, 2F-07FA, and 2F-01A, further highlighting the significance of synchronous regulation of the bulk solvation and interface under high currents and large capacities.

The surface morphology and composition of Zn electrodes cycled at  $1\text{ mA cm}^{-2}$  after 50 cycles in different electrolytes were examined. Note that the cell using the baseline electrolyte prematurely short-circuited along with massive by-products covering the Zn metal and large protrusions entangling the separator (Fig. S36, ESI†). By contrast, the X-ray diffraction (XRD) peaks assigned to by-products are negligible in dual-anion electrolytes. SEM images reveal that the surface of the Zn electrode in the 2F-07A electrolyte is highly homogeneous and densely packed relative to that in 2F-01A and 2F-07FA (Fig. S37, ESI†). The chemical composition of the interfacial layer in dual-anion electrolytes was analyzed using X-ray photoelectron spectroscopy (XPS) with  $\text{Ar}^+$  sputtering (Fig. 5a). For the depth profile of F 1s spectra, the peak can be deconvoluted into inorganic  $\text{ZnF}_2$  ( $\sim 684.7\text{ eV}$ ) and organic  $-\text{CF}_3$  ( $\sim 688.4\text{ eV}$ ) where the ascendancy of  $\text{ZnF}_2$  with extended sputtering time largely arises from the  $\text{OTf}^-$  decomposition. A similar trend can be seen in the S 2p spectra, which can be fitted into  $-\text{CF}_3\text{SO}_3$  ( $\sim 169.5\text{ eV}$ ) and  $\text{ZnS}$  ( $\sim 162.4\text{ eV}$ ). In O 1s spectra, the surface of the interphase is dominated by organic species ( $\text{S}-\text{O}$  or  $\text{C}=\text{O}$ ) at  $\sim 532.8\text{ eV}$  and  $\text{ZnCO}_3$  at  $\sim 532.2\text{ eV}$ . The observation of  $\text{ZnCO}_3$  can be ascribed to the presence of dissolved  $\text{CO}_2$  in the electrolyte and the decomposition of coordinated anions during cycling.<sup>31,48,49</sup> A new peak assigned to  $\text{ZnO}$  or  $\text{Zn}(\text{OH})_2$  ( $\sim 530.6\text{ eV}$ ) appears after etching and gradually dominates the oxygen-containing components over 180 s of etching. In addition, the C 1s spectra display a  $\text{ZnCO}_3$  signal centered at  $\sim 290.0\text{ eV}$  and  $\text{Ac}^-$ -derived  $(\text{ROCO}_2)\text{Zn}$  at  $\sim 288.5\text{ eV}$ . The ratio of  $\text{ZnCO}_3$  to  $(\text{ROCO}_2)\text{Zn}$  increases with the sputtering depth. Thus, it can be concluded that organic components

predominate in the outer layer of the SEI, imparting flexibility to accommodate the volume fluctuation of the electrode, while inorganic compounds occupying the body of the SEI act as a robust armour for protecting the Zn electrode from dendrite growth.<sup>10,49,50</sup> Fig. S38 and S39 (ESI†) illustrate the SEI compositions for 2F-01A and 2F-07FA. It is discernible that the F 1s and S 1s signals from 2F-01A are notably weaker than the others, suggesting that the regulation in the bulk solvation is too weak to generate an anion-derived inorganic SEI.

Time-of-flight secondary-ion mass spectrometry (ToF-SIMS) was conducted to acquire information on the chemical composition and spatial distribution of the SEI formed in 2F-07A and 2F-07FA electrolytes (Fig. 5b and c). The signal of  $\text{ZnO}^-/\text{ZnOH}^-$  species in both electrolytes is apparently stronger than that of  $\text{ZnF}^-$ ,  $\text{CO}_3^-$ , and  $\text{S}^-$  throughout the interphase, verifying that  $\text{ZnO}^-/\text{ZnOH}^-$  is the major component of the SEI. The corresponding SEI thickness in the 2F-07A electrolyte is determined to be  $\sim 399\text{ nm}$ , thinner than that of the 2F-07FA counterpart ( $\sim 608\text{ nm}$ ). The signal intensity of  $\text{ZnO}^-/\text{ZnOH}^-$ ,  $\text{ZnF}^-$ , and  $\text{S}^-$  manifests apparent irregularity in 2F-07FA compared to those in 2F-07A, suggesting that the  $\text{Zn}^{2+}$ -scarce interface is inclined to induce inhomogeneous deposition. The quantitative comparison of the ion fragment within 500 s of etching time and the integral of the component contents in all etched areas (3000 s) (Fig. 5d and Fig. S40 and S41, ESI†) distinctly revealed a lower electrolyte consumption for interphase construction in 2F-07A, which demonstrates Zn-enriched EDL contributes to a dense SEI. Transmission electron microscopy (TEM) was further employed to characterize the composition of the SEI layer formed in 2F-07A, where the lattice fringes of  $\text{Zn}(\text{OH})_2$ ,  $\text{ZnF}_2$  and  $\text{ZnCO}_3$  were observed, in good accordance with XPS and ToF-SIMS results (Fig. S42, ESI†). Fig. 5e schematically illustrates the disparity in SEI evolution with the addition of  $\text{Ac}^-$  and  $\text{TFA}^-$  characterized by different polarities, where the incorporation of strong-polarity  $\text{Ac}^-$  into the baseline facilitates  $\text{Zn}^{2+}$  desolvation and ion adsorption at the interface, favoring the formation of a uniform and compact SEI. Collectively, we conclude two pivotal prerequisites for electrolyte optimization towards dendrite-suppressed and side reaction-moderated cycling behavior at high currents/capacities: (i)  $\text{Zn}^{2+}$  at the interface is able to promptly compensate for the consumption during the electroreduction process, thus averting the extension of deposited Zn into the bulk electrolyte; (ii)  $\text{Zn}^{2+}$ -solvation structure can decompose into a beneficial SEI, isolating electrode-electrolyte contact and inhibiting dendrite growth.

To verify the practical feasibility of the designed dual-anion electrolyte, hybrid supercapacitors were fabricated by coupling Zn foil with an activated carbon (AC) cathode, as schematically illustrated in Fig. 6a. The Nyquist plots of the supercapacitors with 2F-07A show the smallest charge transfer resistance as compared to that of 2F-07FA and the baseline (Fig. 6b), implying the superior charge storage capability of 2F-07A. Fig. 6c shows a comparison of the rate capability of the supercapacitor with different electrolytes at varying rates. As expected, the supercapacitor with 2F-07A harvests a higher capacity of 98.9, 87.8, 74.6, 60.8, and  $56.9\text{ mA h g}^{-1}$  at 0.3, 0.5, 1, 3, and  $5\text{ A g}^{-1}$ ,

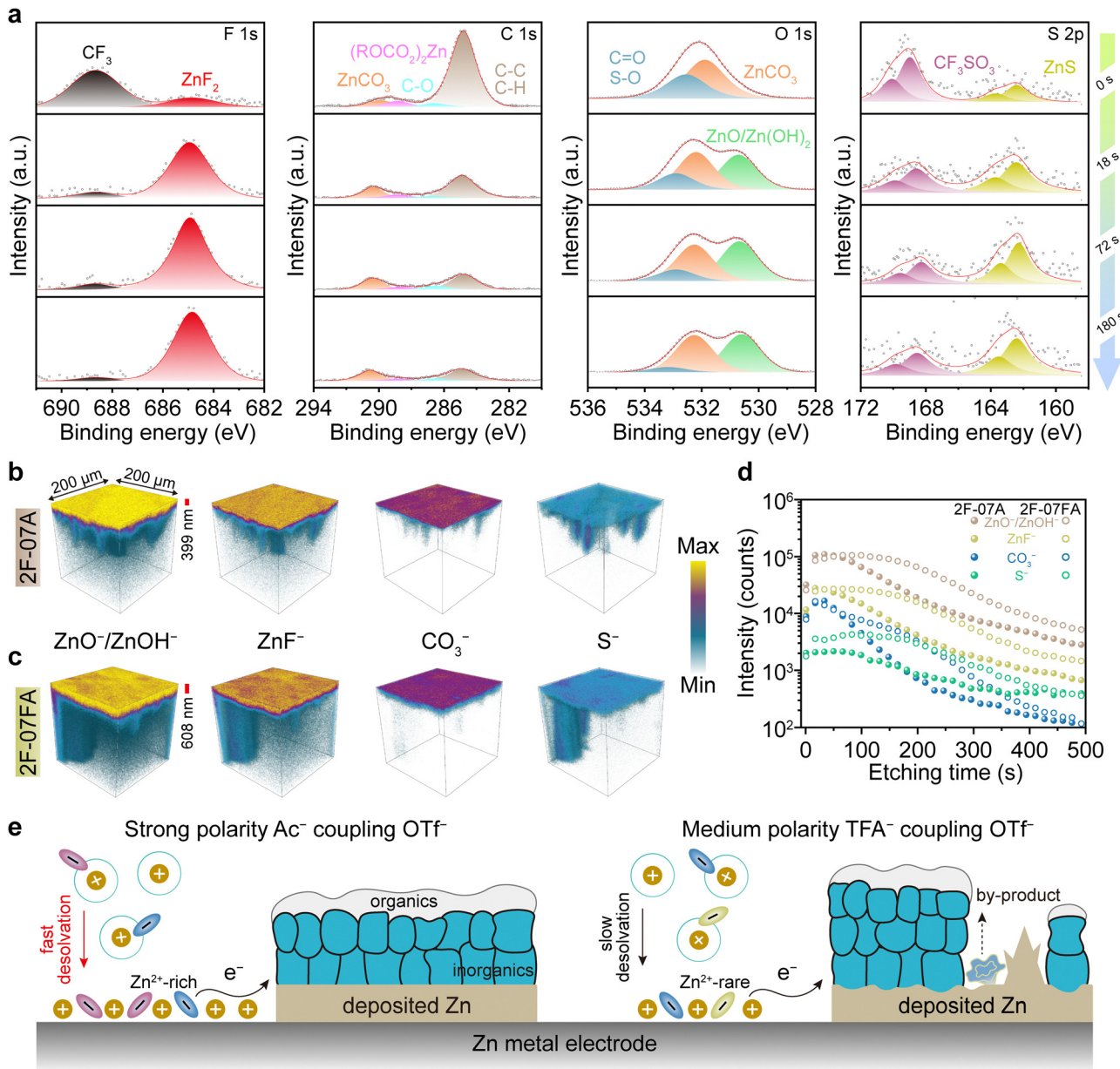


**Fig. 5** Characterization of the dual-anion electrolyte-derived SEI. (a) XPS depth profiles of the Zn surface in a 2F-07A electrolyte at  $1 \text{ mA cm}^{-2}$  after 50 cycles, in the order of F 1s, C 1s, O 1s, and S 2p. 3D reconstruction maps of Zn electrodes retrieved from (b) 2F-07A and (c) 2F-07FA electrolytes measured by ToF-SIMS. (d) Corresponding ToF-SIMS depth profiles of major secondary ions with 2F-07A and 2F-07FA electrolytes. (e) Schematic diagram of SEI generation in the electrolyte of 2F-07A and 2F-07FA with different anion polarities.

respectively, relative to the counterparts. Likewise, the Zn surface in 2F-07A after the rate test is more homogeneous (Fig. S43, ESI†). CV curves of the Zn||AC supercapacitor using 2F-07A show typical capacitive behavior while those using the baseline electrolyte inevitably suffer from side reactions during charging (Fig. S44, ESI†). Furthermore, the 2F-07A electrolyte-based supercapacitor (cathode loading:  $\sim 12 \text{ mg cm}^{-2}$ ) manifests slow capacity attenuation over 3000 cycles. In sharp contrast, the supercapacitor with the baseline electrolyte displays a pronounced capacity decline after 1500 cycles (Fig. 6d and Fig. S45, ESI†).

To meet the practical application, the supercapacitors were further evaluated under harsh conditions of ultrathin thin Zn foil ( $\sim 10 \mu\text{m}$ ) and low N/P (negative capacity to positive capacity: 5). As shown in Fig. 6e, the 2F-07A electrolyte enables the supercapacitor to retain 83% of the initial capacity for 300 cycles, whereas the one with the baseline electrolyte suffers from severe capacity loss, retaining 66% of the initial capacity for 150 cycles. The superior stability in the 2F-07A electrolyte can be attributed to the prompt compensation of Zn<sup>2+</sup> at the interface and dense SEI formation, which effectively inhibit side reactions and dendrite growth. Upon further increasing

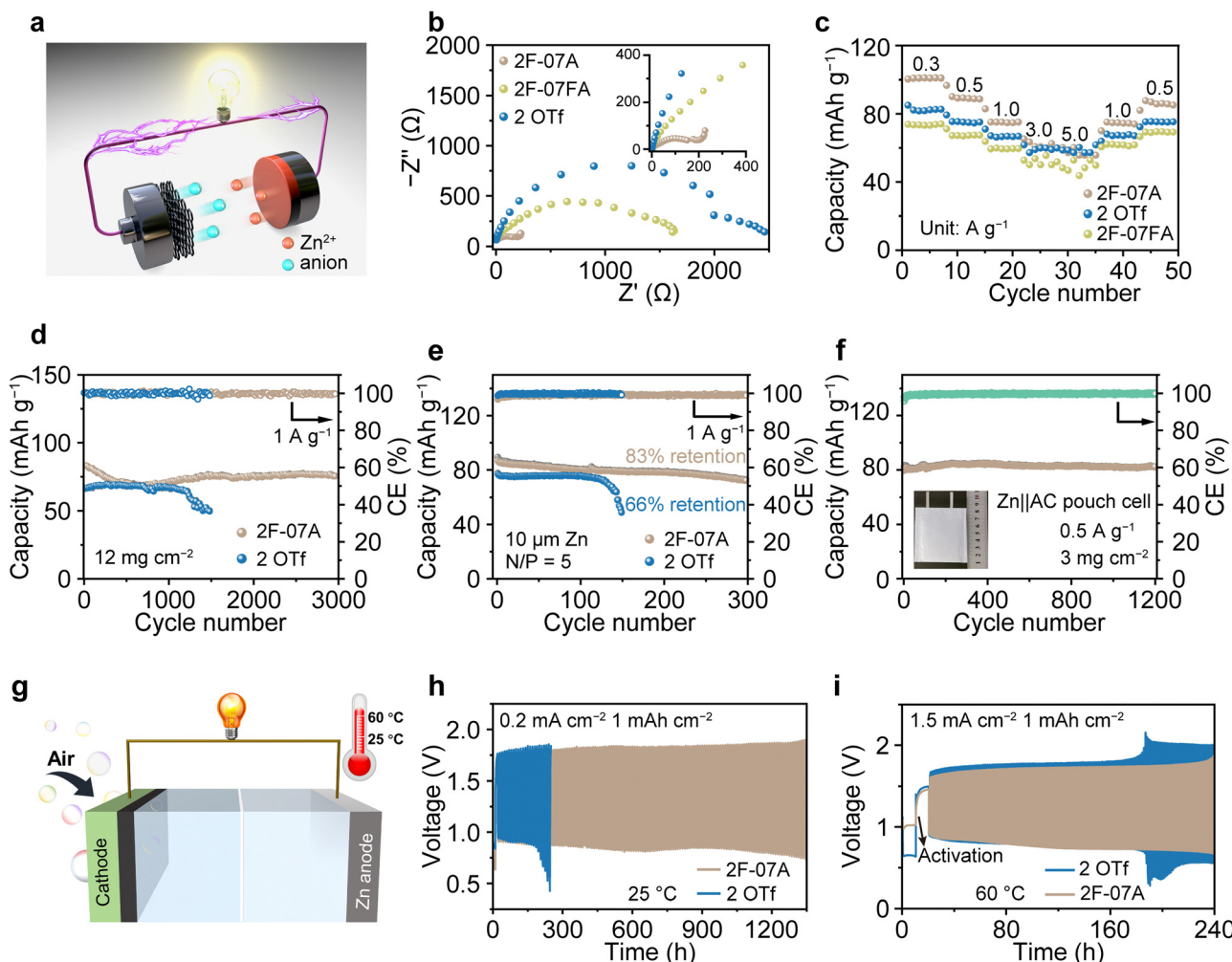


**Fig. 6** Electrochemical performance of Zn||AC hybrid supercapacitors and Zn–air batteries with different electrolytes. (a) Schematic illustration of a Zn||AC supercapacitor. (b) Nyquist plots of the supercapacitors. Inset: Enlarged Nyquist plots in the high frequency range. (c) Rate performance at varying current densities. Galvanostatic cycling performance at 1 A g<sup>-1</sup> with (d) routine Zn foil and (e) thin Zn foil. (f) Pouch-type Zn||AC supercapacitor using a 2F-07A electrolyte at 0.5 A g<sup>-1</sup>. (g) Schematic illustration of a Zn–air battery. Galvanostatic cycling performance of the Zn–air batteries (h) at room temperature and (i) at 60 °C.

the mass loading of the AC cathode up to 18.74 mg cm<sup>-2</sup> with a lean 2F-07A electrolyte (3 µL mg<sup>-1</sup>), a decent capacity retention of 88% over 1500 cycles is achieved (Fig. S46, ESI†). The long-term cycling stability of the pouch-type Zn||AC supercapacitor using 2F-07A is shown in Fig. 6f, delivering a specific capacity of 80 mA h g<sup>-1</sup> at 0.5 A g<sup>-1</sup> with negligible capacity decay over 1200 cycles. To demonstrate the versatility of 2F-07A, Zn–air batteries (ZABs) were also assembled and tested at different temperatures (Fig. 6g). The room-temperature ZAB in 2F-07A exhibits a long lifespan of over 1300 h, far outperforming the battery in the baseline electrolyte that operates within 300 h (Fig. 6h). Even at a high temperature (60 °C), 2F-07A electrolyte-equipped ZAB can sustain an enhanced lifespan (240 h) compared to that in the baseline (180 h) (Fig. 6i), largely arising from the stable and robust interface (Fig. S47, ESI†) and superior water retention capability in the 2F-07A electrolyte (Fig. S48, ESI†).

## Conclusions

In this contribution, we adopt the anion polarity as a general indicator for constructing dual-anion electrolytes in a comparative framework, which screens a dual-anion electrolyte that enables synchronous adjustment of the solvation structure and the EDL towards the durable Zn electrode. The incorporation of strong-polarity Ac<sup>-</sup> into the baseline electrolyte of 2M Zn(OTf)<sub>2</sub> promotes the formation of an anion-enriched solvation shell and a Zn<sup>2+</sup>-enriched condensed interface layer. In addition, the coordinated OTf<sup>-</sup> is capable of decomposing into major constituents of the SEI. Collectively, the dual-anion electrolyte can effectively inhibit dendrite growth and water-induced side reactions, ensuring uniform deposition and long-term operation under high currents and capacities as well as wide temperatures. Impressively, the dual-anion electrolyte with synchronous regulation ability enables the Zn||Zn cell to deliver a cumulative plating capacity of 15.25 A h cm<sup>-2</sup> (3050 h)

at 10 mA cm<sup>-2</sup> and 10 mA h cm<sup>-2</sup>, surpassing state-of-the-art high-capacity Zn electrodes. Furthermore, hybrid Zn<sup>2+</sup> capacitors and Zn–air batteries using the tailored electrolyte manifest improved electrochemical performance. This work sheds light on the polarity combination of anions in synchronous manipulation of bulk solvation and the interfacial EDL, advancing the research of anion chemistry in metal electrode protection.

## Author contributions

R. H. and H. W. conceived the original idea and designed all the experiments. R. H. carried out the experiments and analysed the experimental data with the assistance of W. W., X. L., T. L., Y. L., J. C. and S. C. J. Z. and Q. Z. performed the theoretical calculations. R. H. and H. W. co-wrote the paper. All authors were involved in the discussion of the experimental results and preparation of the manuscript. R. H. and J. Z. contributed equally to this work.

## Conflicts of interest

There are no conflicts to declare.

## Acknowledgements

This work was supported by the Ministry of Science and Technology of China (2021YFA1201900), the National Natural Science Foundation of China (No. 22105107) and the Fundamental Research Funds for the Central Universities.

## Notes and references

- 1 F. Wang, O. Borodin, T. Gao, X. L. Fan, W. Sun, F. D. Han, A. Faraone, J. A. Dura, K. Xu and C. S. Wang, *Nat. Mater.*, 2018, **17**, 543–549.
- 2 L. E. Blanc, D. Kundu and L. F. Nazar, *Joule*, 2020, **4**, 771–799.
- 3 Y. Y. Liu, X. Lu, F. L. Lai, T. X. Liu, P. R. Shearing, I. P. Parkin, G. J. He and D. J. L. Brett, *Joule*, 2021, **5**, 2845–2903.
- 4 N. Zhang, X. Y. Chen, M. Yu, Z. Q. Niu, F. Y. Cheng and J. Chen, *Chem. Soc. Rev.*, 2020, **49**, 4203–4219.
- 5 J. Long, L. Dongmin, X. Xian, J. Dongdong, L. Liwei, L. Le, H. Zhangxing, L. Bingan, L. Shuquan and Z. Jiang, *Energy Storage Mater.*, 2023, **62**, 102932.
- 6 D. H. Wang, Q. Li, Y. W. Zhao, H. Hong, H. F. Li, Z. D. Huang, G. J. Liang, Q. Yang and C. Y. Zhi, *Adv. Energy Mater.*, 2022, **12**, 2102707.
- 7 L. Miao, Z. Xiao, D. Shi, M. Wu, D. Liu, Y. Li, X. Liu, Y. Sun, S. Zhong, Z. Qian and R. Wang, *Adv. Funct. Mater.*, 2023, **33**, 2306952.
- 8 F. Yang, J. A. Yuwono, J. Hao, J. Long, L. Yuan, Y. Wang, S. Liu, Y. Fan, S. Zhao, K. Davey and Z. Guo, *Adv. Mater.*, 2022, **34**, 2206754.
- 9 W. Xu, J. Li, X. Liao, L. Zhang, X. Zhang, C. Liu, K. Amine, K. Zhao and J. Lu, *J. Am. Chem. Soc.*, 2023, **145**, 22456–22465.
- 10 X. Wang, X. Li, H. Fan and L. Ma, *Nano-Micro Lett.*, 2022, **14**, 205.
- 11 L. Cao, D. Li, E. Hu, J. Xu, T. Deng, L. Ma, Y. Wang, X.-Q. Yang and C. Wang, *J. Am. Chem. Soc.*, 2020, **142**, 21404–21409.
- 12 D. Wang, D. Lv, H. Peng, C. Wang, H. Liu, J. Yang and Y. Qian, *Angew. Chem., Int. Ed.*, 2023, **62**, e202310290.
- 13 W. Wang, S. Chen, X. Liao, R. Huang, F. Wang, J. Chen, Y. Wang, F. Wang and H. Wang, *Nat. Commun.*, 2023, **14**, 5443.
- 14 L. Liu, H. Lu, C. Han, X. Chen, S. Liu, J. Zhang, X. Chen, X. Wang, R. Wang, J. Xu, H. K. Liu, S. X. Dou and W. Li, *ACS Nano*, 2023, **17**, 23065–23078.
- 15 C. Huang, X. Zhao, Y. Hao, Y. Yang, Y. Qian, G. Chang, Y. Zhang, Q. Tang, A. Hu and X. Chen, *Energy Environ. Sci.*, 2023, **16**, 1721–1731.
- 16 J. Luo, L. Xu, Y. Zhou, T. Yan, Y. Shao, D. Yang, L. Zhang, Z. Xia, T. Wang, L. Zhang, T. Cheng and Y. Shao, *Angew. Chem., Int. Ed.*, 2023, **62**, e202302302.
- 17 D. Han, Z. Wang, H. Lu, H. Li, C. Cui, Z. Zhang, R. Sun, C. Geng, Q. Liang, X. Guo, Y. Mo, X. Zhi, F. Kang, Z. Weng and Q.-H. Yang, *Adv. Energy Mater.*, 2022, **12**, 2102982.
- 18 G. Duan, Y. Wang, L. Sun, Z. Bao, B. Luo, S. Zheng, Z. Ye, J. Huang and Y. Lu, *ACS Nano*, 2023, **17**, 22722–22732.
- 19 C. Huang, X. Zhao, S. Liu, Y. Hao, Q. Tang, A. Hu, Z. Liu and X. Chen, *Adv. Mater.*, 2021, **33**, 2100445.
- 20 J. Cao, D. Zhang, R. Chanajaree, Y. Yue, Z. Zeng, X. Zhang and J. Qin, *Adv. Powder Mater.*, 2022, **1**, 100007.
- 21 C. Yang, J. Xia, C. Cui, T. P. Pollard, J. Vatamanu, A. Faraone, J. A. Dura, M. Tyagi, A. Kattan, E. Thimsen, J. Xu, W. Song, E. Hu, X. Ji, S. Hou, X. Zhang, M. S. Ding, S. Hwang, D. Su, Y. Ren, X.-Q. Yang, H. Wang, O. Borodin and C. Wang, *Nat. Sustainability*, 2023, **6**, 325–335.
- 22 S. Chen, R. Lan, J. Humphreys and S. Tao, *Energy Storage Mater.*, 2020, **28**, 205–215.
- 23 X. Xu, H. Su, J. Zhang, Y. Zhong, Y. Xu, Z. Qiu, H. B. Wu, X. Wang, C. Gu and J. Tu, *ACS Energy Lett.*, 2022, **7**, 4459–4468.
- 24 S. Chen, D. Ji, Q. Chen, J. Ma, S. Hou and J. Zhang, *Nat. Commun.*, 2023, **14**, 3526.
- 25 H. Yang, D. Chen, R. Zhao, G. Li, H. Xu, L. Li, X. Liu, G. Li, D. Chao and W. Han, *Energy Environ. Sci.*, 2023, **16**, 2910–2923.
- 26 H. Du, Y. Dong, Q.-J. Li, R. Zhao, X. Qi, W.-H. Kan, L. Suo, L. Qie, J. Li and Y. Huang, *Adv. Mater.*, 2023, **35**, 2210055.
- 27 Z. Liu, L. Li, L. Qin, S. Guo, G. Fang, Z. Luo and S. Liang, *Adv. Mater.*, 2022, **34**, 2204681.
- 28 X. Yang, Q. Zhou, S. Wei, X. Guo, P. J. Chimtali, W. Xu, S. Chen, Y. Cao, P. Zhang, K. Zhu, H. Shou, Y. Wang, X. Wu, C. Wang and L. Song, *Small Methods*, 2023, 2301115.
- 29 Y. Sui and X. Ji, *Angew. Chem., Int. Ed.*, 2024, **63**, e202312585.
- 30 T. C. Li, C. Lin, M. Luo, P. Wang, D.-S. Li, S. Li, J. Zhou and H. Y. Yang, *ACS Energy Lett.*, 2023, **8**, 3258–3268.

- 31 D. Dong, T. Wang, Y. Sun, J. Fan and Y.-C. Lu, *Nat. Sustainability*, 2023, **6**, 1474–1484.
- 32 L. Suo, O. Borodin, Y. Wang, X. Rong, W. Sun, X. Fan, S. Xu, M. A. Schroeder, A. V. Cresce, F. Wang, C. Yang, Y.-S. Hu, K. Xu and C. Wang, *Adv. Energy Mater.*, 2017, **7**, 1701189.
- 33 Y. Dong, L. Miao, G. Ma, S. Di, Y. Wang, L. Wang, J. Xu and N. Zhang, *Chem. Sci.*, 2021, **12**, 5843–5852.
- 34 F. Ming, Y. Zhu, G. Huang, A.-H. Emwas, H. Liang, Y. Cui and H. N. Alshareef, *J. Am. Chem. Soc.*, 2022, **144**, 7160–7170.
- 35 T. Wang, H. Cheng, Z. Tian, Z. Li, Z. Lin, Z. You, Y. Lu, Y. Zhu, W. Li, Y. Yang, Q. Zhong and Y. Lai, *Energy Storage Mater.*, 2022, **53**, 371–380.
- 36 P. Xiao, Y. Wu, J. Fu, J. Liang, Y. Zhao, Y. Ma, T. Zhai and H. Li, *ACS Energy Lett.*, 2023, **8**, 31–39.
- 37 B. Niu, Z. Li, D. Luo, X. Ma, Q. Yang, Y.-E. Liu, X. Yu, X. He, Y. Qiao and X. Wang, *Energy Environ. Sci.*, 2023, **16**, 1662–1675.
- 38 Y. Lv, M. Zhao, Y. Du, Y. Kang, Y. Xiao and S. Chen, *Energy Environ. Sci.*, 2022, **15**, 4748–4760.
- 39 Z. Wang, M. Zhou, L. Qin, M. Chen, Z. Chen, S. Guo, L. Wang, G. Fang and S. Liang, *eScience*, 2022, **2**, 209–218.
- 40 T. Abe, H. Fukuda, Y. Iriyama and Z. Ogumi, *J. Electrochem. Soc.*, 2004, **151**, A1120–A1123.
- 41 C. Yan, H.-R. Li, X. Chen, X.-Q. Zhang, X.-B. Cheng, R. Xu, J.-Q. Huang and Q. Zhang, *J. Am. Chem. Soc.*, 2019, **141**, 9422–9429.
- 42 K. Xu, A. von Cresce and U. Lee, *Langmuir*, 2010, **26**, 11538–11543.
- 43 H. Li, Y. Ren, Y. Zhu, J. Tian, X. Sun, C. Sheng, P. He, S. Guo and H. Zhou, *Angew. Chem., Int. Ed.*, 2023, **62**, e202310143.
- 44 X. Yang, W. Li, Z. Chen, M. Tian, J. Peng, J. Luo, Y. Su, Y. Zou, G. Weng, Y. Shao, S. Dou and J. Sun, *Angew. Chem., Int. Ed.*, 2023, **62**, e202218454.
- 45 L. Wang, C. Shen, C. Huang, J. Chen and J. Zheng, *ACS Nano*, 2023, **17**, 24619–24631.
- 46 Y. Yang, H. Yang, R. Zhu and H. Zhou, *Energy Environ. Sci.*, 2023, **16**, 2723–2731.
- 47 B. D. Adams, J. Zheng, X. Ren, W. Xu and J.-G. Zhang, *Adv. Energy Mater.*, 2018, **8**, 1702097.
- 48 D. Li, L. Cao, T. Deng, S. Liu and C. Wang, *Angew. Chem., Int. Ed.*, 2021, **60**, 13035–13041.
- 49 J. Hao, B. Li, X. Li, X. Zeng, S. Zhang, F. Yang, S. Liu, D. Li, C. Wu and Z. Guo, *Adv. Mater.*, 2020, **32**, 2003021.
- 50 Y. Li, Z. Yu, J. Huang, Y. Wang and Y. Xia, *Angew. Chem., Int. Ed.*, 2023, **62**, e202309957.